Faraday Discussions

Accepted Manuscript

This manuscript will be presented and discussed at a forthcoming Faraday Discussion meeting. All delegates can contribute to the discussion which will be included in the final volume.

Register now to attend! Full details of all upcoming meetings: http://rsc.li/fd-upcoming-meetings

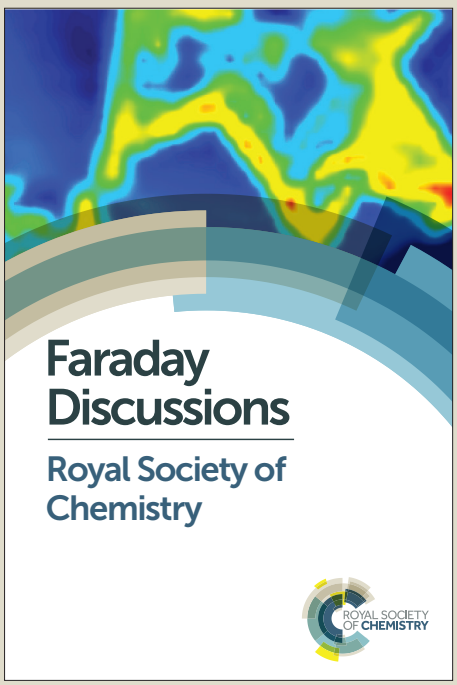

This is an *Accepted Manuscript*, which has been through the Royal Society of Chemistry peer review process and has been accepted for publication.

Accepted Manuscripts are published online shortly after acceptance, before technical editing, formatting and proof reading. Using this free service, authors can make their results available to the community, in citable form, before we publish the edited article. We will replace this *Accepted Manuscript* with the edited and formatted *Advance Article* as soon as it is available.

You can find more information about *Accepted Manuscripts* in the Information for Authors.

Please note that technical editing may introduce minor changes to the text and/or graphics, which may alter content. The journal's standard Terms & Conditions and the Ethical guidelines still apply. In no event shall the Royal Society of Chemistry be held responsible for any errors or omissions in this *Accepted Manuscript* or any consequences arising from the use of any information it contains.

ROYAL SOCIETY OF CHEMISTRY

www.rsc.org/faraday_d

Faraday Discussions

PAPER

Advancements in quantum cascade laser-based infrared microscopy of aqueous media

[1]Received 00th January 20xx,
Accepted 00th January 20xx

DOI: 10.1039/x0xx00000x

www.rsc.org/

K. Haase‡[a], N. Kröger-Lui‡[a], A. Pucci[a], A. Schönhals[a] and W. Petrich[a]

The large mid-infrared absorption coefficient of water frequently hampers the rapid, label-free infrared microscopy of biological objects in their natural aqueous environment. However, the high spectral power density of quantum cascade lasers is shifting this limitation such that mid-infrared absorbance images can be acquired in situ within signal-to-noise ratios of up to 100. Even at sample thicknesses well above 50 µm signal-to-noise ratios above 10 are readily achieved. The quantum cascade laser-based microspectroscopy of aqueous media is exemplified by imaging an aqueous yeast solution and quantifying glucose consumption, ethanol generation as well as the production of carbon dioxide gas during fermentation.

1 Introduction

Spectroscopy in the mid-infrared spectral region can be used for label-free and quantitative measurements of biomolecules, such as carbohydrates, DNA or proteins. However, when trying to investigate biological objects in their natural habitat the high mid-infrared absorption coefficient of water constitutes a challenging obstacle.

Mid-infrared microspectroscopic studies of individual live cells in aqueous environments have been reported more than a decade ago.[1] These measurements were performed using a FT-IR spectrometer with globar source and a water layer thickness of 10 µm. Further studies of live cells in aqueous media as well as microfluidic events based on FT-IR-spectroscopy with a globar were conducted at path length of 10-25 µm.[2-5] Shortly after the first studies of cells in aqueous media using globar-based FT-IR microspectroscopy, Moss et al. investigated cell cultures and single cells under aqueous media using synchrotron radiation-based FT-IR micro-spectroscopy, with a measured path length of 11-12 µm. For the first time, cell division and motility were observed during the FT-IR experiment.[6]

Microfabricated sample holders have been developed to investigate single cells in aqueous solutions using synchrotron-based FT-IR microspectroscopy at path length of up to 12 µm. For larger cells, measurements were performed using a conventional flow cell with spacers for nominal path lengths of 7.6 µm and 12.7 µm.[7] To monitor arsenic-induced changes to intracellular biomolecules in live leukemia cells, synchrotron-based FT-IR-microspectroscopy was performed at path length of less than 10 µm.[8] In more recent studies, synchrotron-based FT-IR microspectroscopy was used to observe the progression of fibroblast cells through the cell cycle.[9] Further information is provided in, for example, ref. 10 and ref. 11.

The recent progress in quantum cascade laser (QCL)[12] technology allows for the rapid investigation of samples at water layer thicknesses well above 10 µm. QCLs have been successfully used, for example, in non-imaging mid-infrared spectroscopy-based sensor systems to determine the concentration of glucose in aqueous solutions in vitro.[13] Furthermore, measurements of glucose concentration in human blood serum were performed using a flow cell with a liquid layer thickness of 140 µm together with a highly sensitive, liquid-nitrogen cooled detector, whereby a root mean square error of prediction of 6.9 mg/dL was achieved.[14] More recently, protein concentration and secondary structure in water have been determined using a QCL-based setup with a flow cell with 38 µm liquid layer thickness.[15] Finally, fibre-based QCL sensors enabled the continuous, minimally invasive quantification of glucose in the interstitial fluid of subcutaneous tissue of rats in vivo.[16]

QCLs have also been used for infrared microscopy in order to increase measurement speed whilst maintaining a reasonable signal-to-noise ratio.[17-20] The rapid investigation of thin tissue sections using QCL-based infrared microscopes has been demonstrated for selected spectral regions.[21,22] The investigation of infrared absorption at pre-selected, discrete frequencies can speed up the hyperspectral imaging of thin tissue sections even further.[22-24] Microscopic imaging at a single mid-infrared wavelength can be performed even in real time using QCL-based microscopes, as was recently demonstrated using living microorganisms in a measurement chamber with a water layer thickness of 25 µm and at a framerate of 50 Hz.[25]

[a] Heidelberg University, Kirchhoff Institute for Physics, Im Neuenheimer Feld 227, 69120 Heidelberg, Germany.
‡ These authors contributed equally to this work.
See DOI: 10.1039/x0xx00000x

Ultimately, the feasibility and performance of QCL-based microscopy is governed by the ratio between the obtainable signal and the noise. Hence, in this manuscript the aspect of signal-to-noise is defined, analysed and interpreted. QCL-based microspectroscopy of a biologically active aqueous sample is illustrated on the example of a fermentation process.

2 Materials and methods

All infrared measurements described here are conducted with a custom built, QCL-based infrared microscope (Fig. 1). For illumination of the sample a QCL (type CW-MHF, Daylight Solutions Inc., San Diego, USA) can be tuned over the spectral region of 1027-1087 cm^{-1} within less than 12 seconds. The calibration of laser output power as well as wavelength can be performed in parallel to infrared microscopy. The microscope is using an uncooled microbolometer array detector (VarioCam hr head, InfraTec GmbH, Dresden, Germany) with 640 x 480 pixel elements and a pixel pitch of 25 µm for infrared measurements in transmission mode. For large objects, lens optics for a nominal magnification of 1:1 can be chosen. The optical resolution in 1:1 magnification was determined to be 23.0 ± 3.5 µm for a field of view of 10.6 x 11.7 mm^2. A more detailed description of the setup can be found in ref. 20.

For infrared transmission measurements of samples in aqueous solutions, a custom built cuvette (Fig. 2) was mounted on the microscopy stage of the infrared microscope. The cuvette consists of two barium fluoride windows (Korth Kristalle GmbH, Altenholz, Germany) and an exchangeable mylar or PTFE spacer (Specac Ltd, Kent, England) determining the water layer thickness of the measurement chamber. The cuvette is equipped with a heating element (Omega Engineering Limited, United Kingdom) and a temperature sensor (PT100, Heraeus, Germany) enabling temperature control by a digital PID controller (ETC8420, ENDA, Germany).

In order to discuss signal-to-noise levels, the transmission of the water-filled cuvette is referenced to the transmission signal of the empty cuvette, thus enabling the calculation of absorbance. By fitting a model for the absorbance of water to the spectra in each pixel, one can estimate the noise in each pixel by the root mean square deviation between the data points and the fit. We followed the quantification of noise provided in ref. 26. More precisely, the 'single-pixel noise' can be estimated by dividing the mean transmission by the root mean square error of the fit. It is important to note that pixel-to-pixel variations among the spectra of neighbouring pixels in an image will not contribute to the single-pixel noise. Hence, for a more detailed analysis of noise in imaging applications, analysis of the deviation of pixel count rates within an image is important.[24]

The in-situ measurements of biologically active fluids were performed in two different configurations:

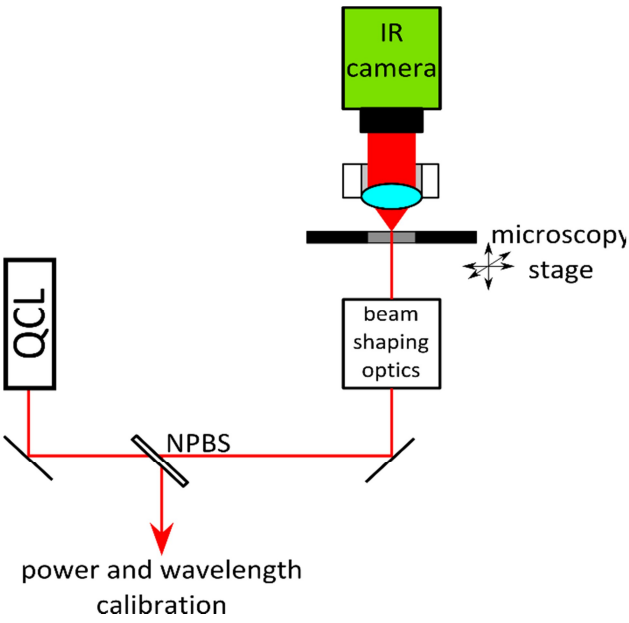

Figure 1: Schematic of the QCL-based infrared microscope. The laser beam originates from a tunable QCL (1030-1090 cm^{-1}) and is directed towards a non-polarizing beam splitter (NPBS). Power and wavelength of the QCL can be monitored parallel to microscopy. The magnification of the microscope was chosen to be 1:1 (with 10.6x11.7 mm^2 field of view and 23.0±3.5 µm pixel pitch) by selection of a macro lens in front of the microbolometer array detector. Adjustable beam shaping optics can be used to, for example, limit the QCL illumination to the size of the field of view of the detector.[20]

(1) In the first configuration 2 µL of solution were dispensed onto the lower BaF_2 window of the chamber. A 1 mm thick PTFE spacer was used such that the droplet did not get in touch to the upper BaF_2 window. The primary sealing of the cuvette by the spacer is supposed to prevent the solution from evaporating out of the chamber. The chamber was investigated for about 9 h taking data every 30 min while the temperature was constantly held at 35.0 ± 0.5 °C. Each acquisition circle was performed averaging over 20 laser sweep scans leading to a measurement time < 10 min. The image data was referenced to a measurement without any object in the beam path. The inhomogeneous thickness of the solution droplet due to its free shape was taken into account by spatially distinguishing pixels containing solution and pixels that are background via an upper (T = 0.5) and lower (T = 0.08) threshold in the transmission T. The spectra were then averaged over the region assigned to solution and investigated using a pure component analysis.

(2) In the second configuration a Mylar spacer with a thickness of 12 µm was used and the chamber was

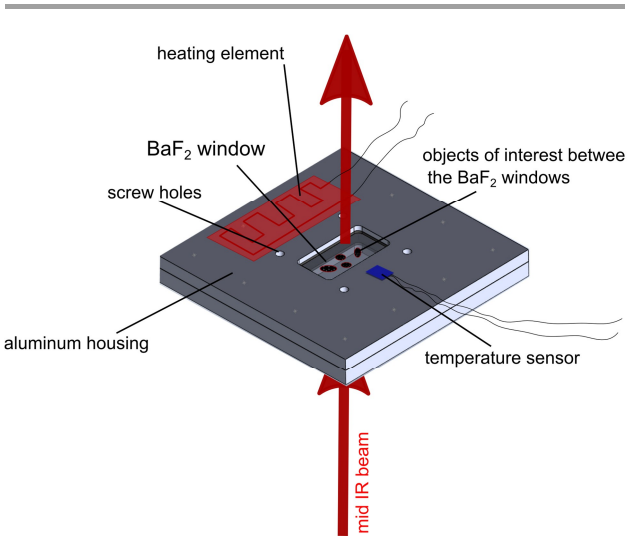

Figure 2: Schematic of the cuvette design. Barium fluoride windows are separated by a Mylar or PTFE spacer. The volume of the cuvette is sealed using an O-ring, which is placed between the barium fluoride windows and the aluminium housing. The cuvette temperature is controlled using a temperature sensor and a heater plus the respective electronic circuitry.

completely filled with solution. In this setting, the CO_2 created during the fermentation process generates gas bubbles within the liquid. In a later stage, smaller bubbles agglomerate to form larger areas of CO_2 such that the volume of CO_2 can be derived from the infrared transmission image by means of a thresholding followed by a convex hull segmentation. In this way, a simultaneous monitoring of glucose, ethanol as well as CO_2 can be performed.

For either of the configurations we monitored a fermentation process as an example in that the measurement chamber was filled with a solution of the following constituents: 0.5 g/dL Yeast (Saccharomyces cerevisiae, Alcotec, United Kingdom), 1 g/dL LB medium (LB Broth, Sigma Aldrich, Germany), 2 g/dL glucose (D(+)Glucose, Merck KGaA, Germany).

3 Results and Discussion

In order to elucidate the feasibility of and conditions for imaging living matter, two series of measurements were performed in the course of the experiments described here, one targeting the signal-to-noise aspects of the QCL-based microspectroscopy and a second one to illustrate the application capabilities.

3.1 Signal and noise

In a first series of measurements the cuvette was filled with water of varying thickness. The average transmission of water in the spectral range of the QCL ranges from 54.1 % ± 0.8 % to 2.8 % ± 0.3 % for water thicknesses between 6 µm and 50 µm, respectively[+]. The analysis of the thickness-dependence yields an extinction coefficient of 685 /cm. Since scattering of the MIR radiation in the thin water layer is negligible, the extinction coefficient is identical to the absorption coefficient and agrees with the data reported in literature (see e.g. ref. 27) within the error margins.

The spectral dependence of the raw signal of e.g. the IR camera's center pixel is shown for the case of the empty cuvette in Fig. 3. The comparison between this signal and the raw signal obtained through a cuvette filled with a water layer of 6 µm thickness reveals that the spectral shape of the raw signal is governed by the wavenumber-dependence of the laser output power ("gain profile").

When assuming that the spectral dependence of transmission through water can be approximated by a moderate, but linear spectral dependence of e.g. 0.0002/cm^{-1} (dashed line in Fig. 3b), the difference between the actual transmission at any wavenumber and this linear fit may be used as an estimate for the noise as detected by the pixel.

We here define "noise" as the deviation between a measured signal y_i and a reference y_{ref} according to

$$N = \sqrt{\frac{1}{n-1}\sum_{i=1}^{n}\left(y_i - y_{ref}\right)^2}$$

In the case of **single-pixel noise N_s**, we refer to the transmission signal at any given wavenumber as y_i and the corresponding value of the linear approximation to the wavenumber dependence, i.e. the dashed line in Fig. 3b, as y_{ref}. The sum then averages the squares of these deviations over n wavenumber intervals within a given wavenumber range under consideration. For the data in Fig. 3, for example, the corresponding single-pixel noise N_s of the transmission amounts to 0.37 % for the full spectral tuning range of the QCL (1027 cm^{-1} – 1087 cm^{-1}) and to 0.32 % for the more intense and central part of the spectrum, i.e. between 1041 cm^{-1} and 1079 cm^{-1}.

In contrast to the single-pixel analysis of the noise, the pixel-to-pixel variation has to be considered in an imaging scenario, too: Even if the single-pixel noise would be close to zero, an image may still look "noisy" under constant illumination. Hence, the single-pixel noise provides a lower limit for the overall noise of an image and the pixel-to-pixel variation might add to the imaging noise. We therefore evaluate the noise among the pixels as a further measure for noise and hereby refer to it as **pixel-to-pixel noise**[++] **N_{pp}**. The pixel-to-pixel noise

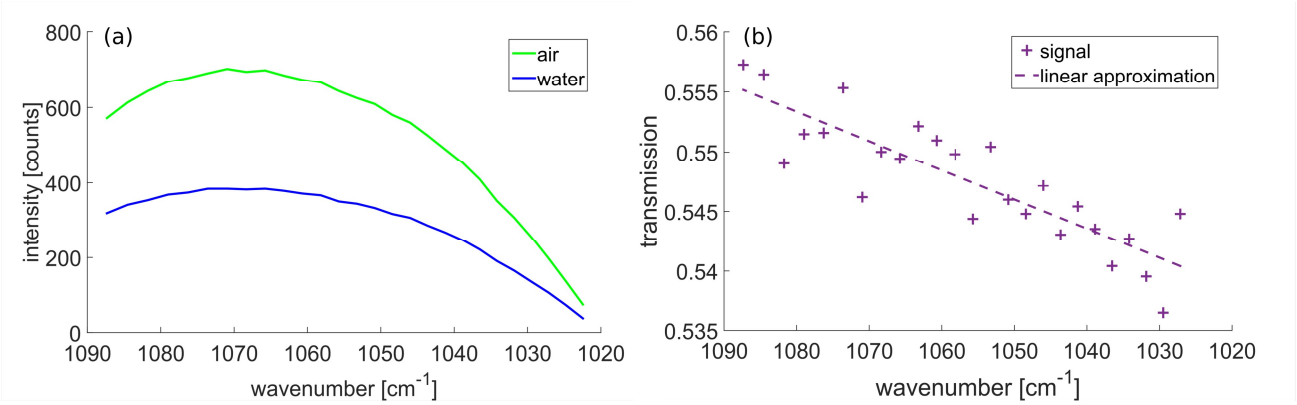

Figure 3: (a) Single-pixel raw signal originating from the transmitted laser radiation during a laser sweep for the case of an air-filled (green) and a water filled (blue) cuvette with layer thickness 6 µm. (b) The ratio of these two measurements reveals the transmission of approximately 54% in agreement with the expectations from literature. The dashed line indicates the very moderate wavenumber-dependence of the transmission through water, which may be approximated by a simple linear function.

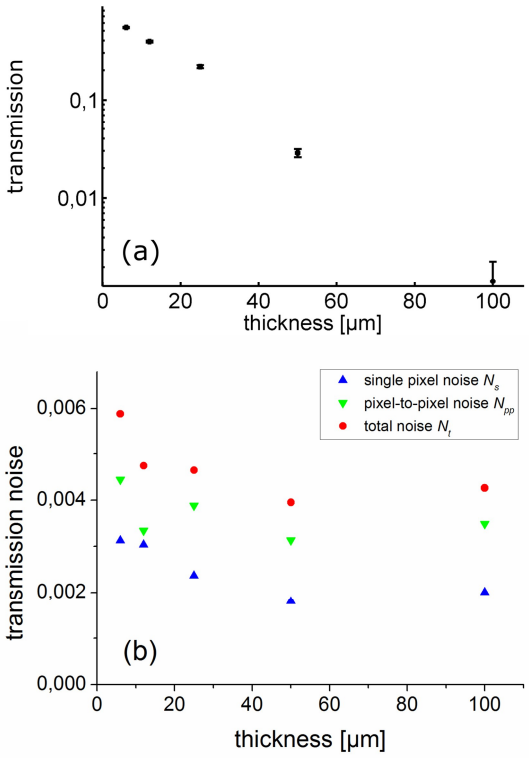

Figure 4: (a) Transmission and (b) its various noise contributions as a function of layer thickness. The data shown is taken from a 9x9 pixel region in the centre of the measurement window and is averaged over the spectral range from 1041 cm^{-1} – 1079 cm^{-1}.

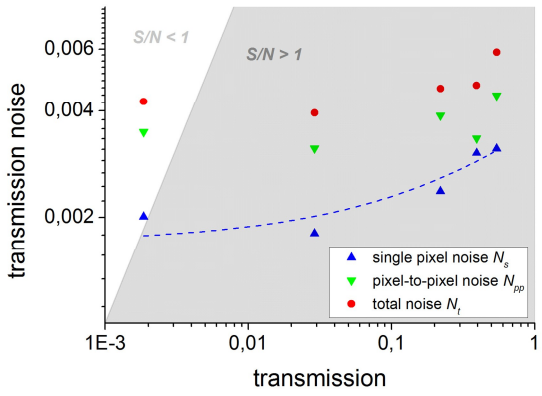

Figure 5: The transmission noise as a function of the transmission based on the data shown in Fig. 4. The shaded area marks the region for which the signal-to-noise ratio is larger than 1. A square root relationship above the background noise is sketched for the example of single-pixel noise (dashed line).

is calculated according to the above formula, whereby a field of m pixels is considered as follows: Given the negligible wavelength dependence of the transmission through water over the given tuning ranges, we take the spectral average of the transmission at any pixel as y_i and the common average of y_i over all m pixels as y_{ref}. For the data shown in Fig. 3, for example, the pixel-to-pixel noise N_{pp} of the transmission amounts to 0.45 % for the full and 0.40 % for the central part of the spectral tuning range.

Finally, the combination of the inherent noise in each pixel N_s and the deviations among the pixels N_{pp} provides an estimate for what we dubbed the **total noise N_t**, which is calculated by comparing the signal of each pixel at any given wavenumber (y_i) to the overall mean of these signals averaged among the m

thickness [µm]	average transmission	single pixel		pixel-to-pixel		total	
		full	limited	full	limited	full	limited
6	0.54	145.4	168.1	121.2	137.2	91.3	106.6
12	0.39	109.4	125.1	115.8	125.8	81.8	94.4
25	0.22	73.5	89.9	55.7	65.3	46.6	56.0
50	0.029	11.5	15.6	9.0	10.5	7.2	8.9
100	0.0019	0.5	0.9	0.4	0.6	0.3	0.5

Table 1: Signal-to-noise ratios of transmission for different layer thicknesses, methods of noise calculation, and spectral ranges (full: 1027 cm^{-1} – 1087 cm^{-1}; limited: 1041 cm^{-1} – 1049 cm^{-1}) based on a 9x9 pixel sample.

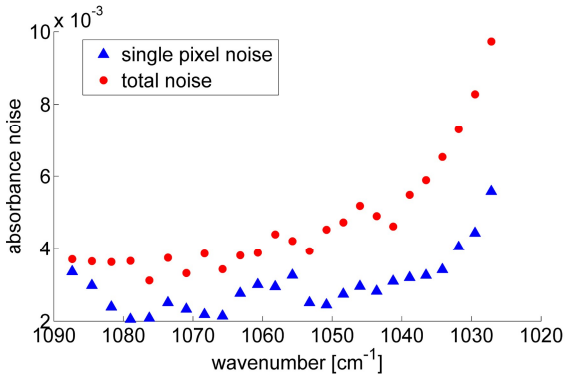

Figure 6: Spectral dependence of the single-pixel noise and the total noise of the absorbance. The noise reaches its minimum in the spectral range of the maximum of the laser gain profile, suggesting that the noise is intensity dependent.

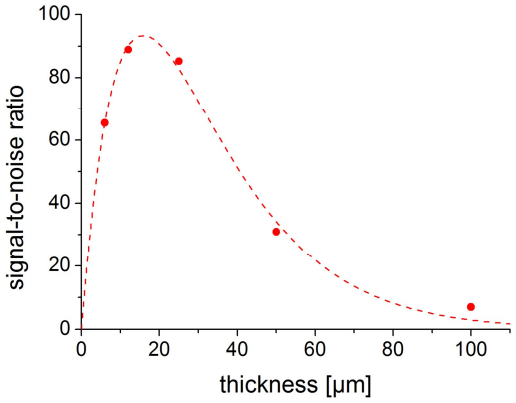

Figure 7: Signal-to-noise ratio in terms of absorbance signal and total noise as a function of thickness of the water layer. The dashed line indicates the theoretical trend.

pixels under consideration (y_{ref}). The total noise N_t of the transmission equals 0.59 % and 0.51 % for the spectral ranges of 1027 cm^{-1} – 1087 cm^{-1} and 1041 cm^{-1} – 1079 cm^{-1}, respectively, for the data shown in Fig. 3.

The spectrally averaged transmission as well as the single pixel noise, the pixel-to-pixel noise and the total noise are shown in Fig. 4 for the various thicknesses of the water layer.
The transmission noise decreases with decreasing signal (i.e. increasing thickness of the absorbing water layer) down to a level of ~0.2 % for the single pixel noise. The heterogeneity among the pixels leads to a noise floor of ~0.3 %, which overall can be summarized as a total noise background for transmission around 0.4 %. Further analysis shows that the noise approximately follows the expected square root dependence on the transmission (plus the constant noise floor) and provides sufficient signal as compared to the noise even for thicknesses well above 50 µm (Fig. 5). This, in turn, means that in our setup transmission measurements can be performed in aqueous solutions for thicknesses well above 50 µm, whereby even at 50 µm the signal is still approximately 10 times larger than the noise. The complete list of average transmission signals as well as the signal-to-noise ratios for the various noise sources are provided as a function of thickness of the water layer in Table 1.

While the analysis of the transmission *T* enables a better understanding of the origin of the noise and the fundamental limitations, the investigation of the noise in terms of the absorbance *A* is of a more practical importance. As an example for the absorbance noise, the spectral dependence of the single-pixel noise and the total noise are displayed in Fig. 6 for the case of a 6 µm thick water layer. In either case, the absorbance noise reaches its respective minimum of 0.002 and 0.004 in that wavenumber range at which the gain profile is at its maximum (see also Figure 3). This finding suggests that the noise is intensity dependent as already speculated from the above discussion of the transmission data.

In the light of the fundamental differences between absorbance noise and transmission noise, it is important to point out that the loss of transmission is of most interest in practice rather than the transmission itself. In other words and as is well known in this field, the highest transmission (short path lengths) is therefore not desirable since it offers no absorbance signal of the analyte under investigation, while at the same time investigations at very low transmission (large path lengths) are impaired by noise. Hence, the optimum balance between signal gain and noise increase, i.e. the optimum signal-to-noise ratio (S/N) is sought. The absorbance S/N *(A/dA)* and the transmission S/N *(T/dT)* are related by:

thickness [µm]	average absorbance	single pixel		pixel-to-pixel		total	
		full	limited	full	limited	full	limited
6	0.27	88.4	101.9	74.1	83.7	55.9	65.1
12	0.41	101.0	115.2	108.6	117.6	76.7	88.3
25	0.66	108.9	132.8	84.6	98.8	70.6	84.7
50	1.54	33.2	49.8	29.3	36.4	23.0	30.8
100	2.71	10.4	10.7	9.8	9.6	6.7	6.9

Table 2: Signal-to-noise ratios of absorbance for different layer thicknesses, methods of noise calculation, and spectral ranges (full: 1027 cm^{-1} – 1087 cm^{-1}; limited: 1041 cm^{-1} – 1049 cm^{-1}) based on a 9x9 pixel sample.

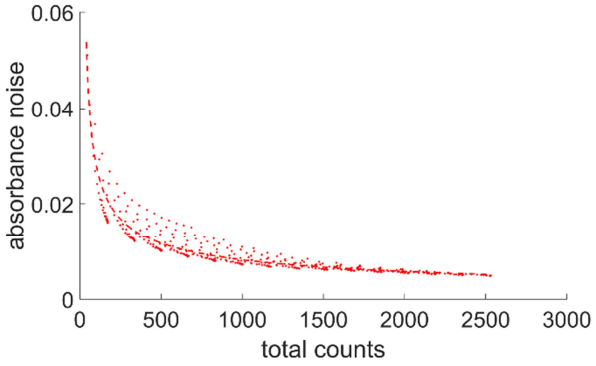

Figure 8: The absorption signal-to-noise ratio shows a clear dependence on the mean intensity. The counts are varied along the gain profile of the laser as well as by averaging over successive frames. The dashed line indicates a ~(c+c0)$^{-0.5}$ dependence.

$$\frac{A}{dA} = \frac{-\log(T)}{-dT/_T} = \log(T)\,\frac{T}{dT}$$

While both the transmission S/N and the absorbance S/N decrease with increasing sample thickness for large thicknesses, it is of note that transmission S/N decreases while the absorbance S/N increases with increasing sample thickness for small thicknesses. The corresponding values for absorbance and the various signal-to-noise ratios are provided in Table 2 for the respective sample thicknesses.

An example for the experimental data is given in Fig. 7. The optimum balance between gain in absorbance signal and increase in noise with increasing sample thickness appears to be around 20 µm for our setup which agrees well with our prior estimates.[28] The single-pixel as well as the pixel-to-pixel noise also peak around that thickness.

Since the signal-to-noise ratio is dependent on laser intensity and, thus, on the overall counts *c* detected by each individual pixel, the S/N may be further improved by averaging over

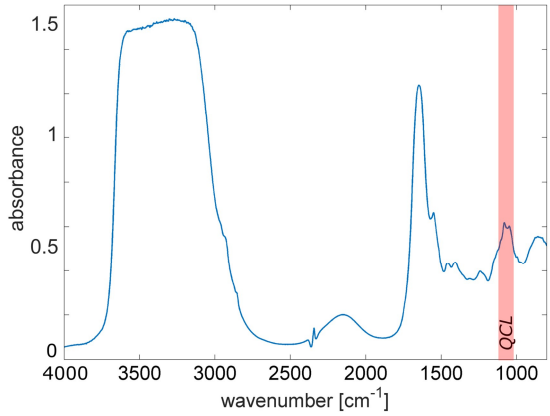

Figure 9: FT-IR spectrum of the fermentation solution.

successive frames for applications, in which the time resolution is less critical than the S/N. When averaging over e.g. 5 successive frames, the absorbance noise is found to decrease by a factor of around 2. In this context, it is interesting to investigate the noise (e.g. the total absorbance noise) as a function of the overall count rate, which changes over the tuning range as well as when averaging over successive measurement frames. Since the spectral dependence of the water absorption in this range is negligible, the main effect upon tuning will be the laser intensity variation over the gain profile. Indeed, the (e.g. total absorbance) noise depends on the laser intensity as well as on the number of frames used for averaging as expected ~(c+c_0)$^{-0.5}$ whereby c_0 is the dark count rate mentioned above (Fig. 8).

3.2 Application example

In order to exemplify the capability of QCL-based mid-infrared microspectroscopy, a fermentation process was studied with respect to glucose consumption, ethanol generation and CO_2 production according to

$$C_6H_{12}O_6 \rightarrow 2C_2H_5OH + 2CO_2$$

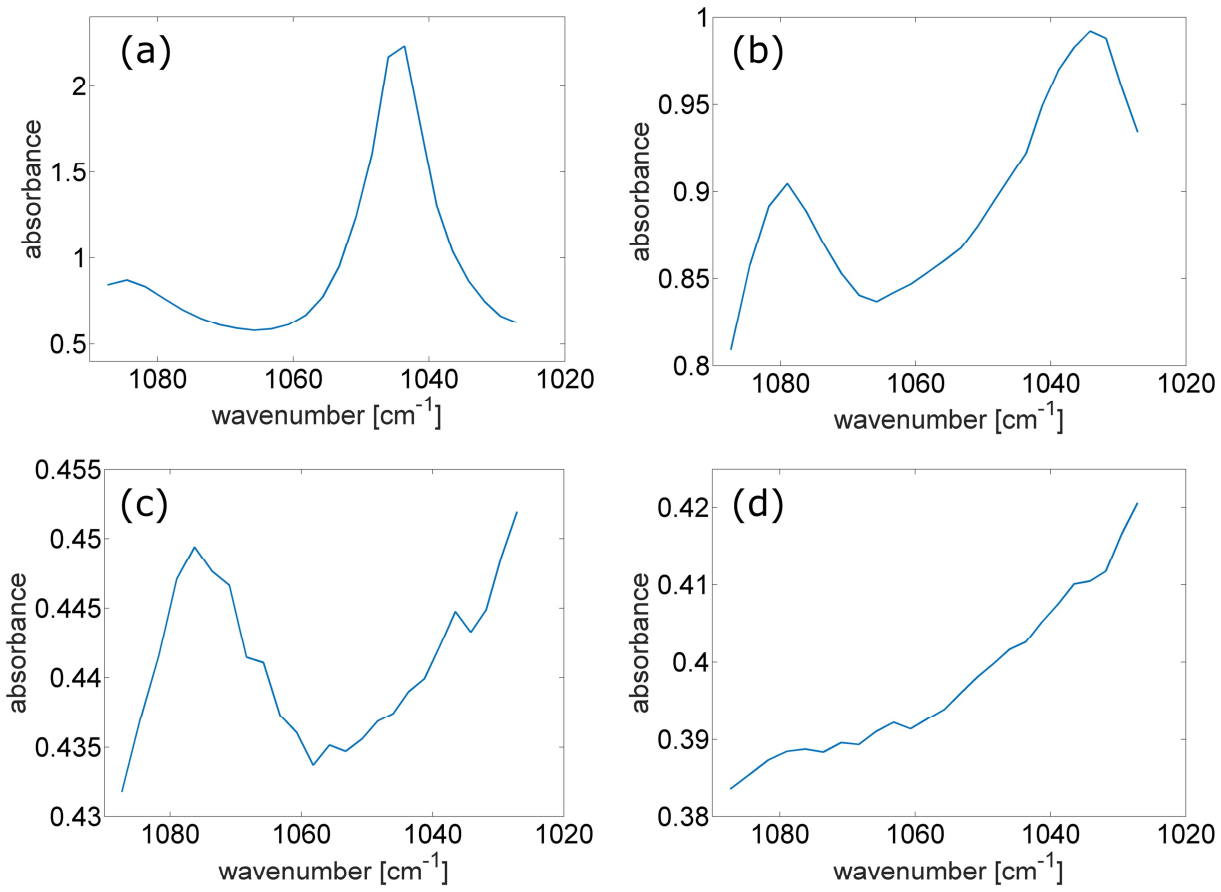

Figure 10: Pure component spectra of (a) ethanol, (b) glucose, (c) yeast and (d) LB medium. The error bars amount to 0.05 for (a), 0.06 for (b), 0.03 for (c) and 0.03 for (d).

A Fourier-transform Infrared (FT-IR) spectrum of the fermentation solution (Fig. 9) was acquired using a standard FT-IR spectrometer (Tensor 27, Bruker Optik GmbH, Germany) and it indicates, that our QCL's tuning range may already suffice for the quantitative investigation of the fermentation process. This tuning range in particular includes the C-O-H vibration band of glucose as well as the C-O stretching vibration of ethanol.

The QCL-based experiment was performed in the two ways mentioned above. For the case in which a droplet of solution was allowed to exchange vapour and gas with the surrounding, it is important to know that the absorbance of the IR-active absorption band of gaseous CO_2 within the tuning range of the QCL is well below 10^{-3} due to the short layer thickness and the low density of the gas. Hence, it can be assumed that contributions of CO_2 to the overall signal are negligible in terms of infrared absorption and it can be shown that this finding holds true also in terms of pressure increase and water displacement. At the same time, the initial evaporation of water from the liquid droplet will came to a halt very rapidly since the small volume inside the cuvette will be saturated with water vapour already by 4 nL of liquid water (35 °C).

The pure component spectra of glucose, ethanol, yeast and LB medium were determined in an independent series of measurements (Fig. 10) with the microscope setup. These spectra of the relevant constituents can be used to analyse the time evolution of the fermentation solution (Fig. 11) in which the changes from a glucose-like spectrum towards an ethanol-like spectrum are evident. The result of a pure component analysis is shown in Fig. 12. Since the height of the droplet is not known, no absolute values for the concentrations can be provided other than average mass and volume concentration per area for glucose and ethanol, respectively. The increase in ethanol concentration follows the decrease in glucose concentrations for the first 5 hours of the experiment as expected. All glucose appear to be consumed after 5 hours which is in agreement with the estimation of the glucose consumption rate of the fermentation at a temperature of 35°C. It is of note, however, that the cuvette seems to become

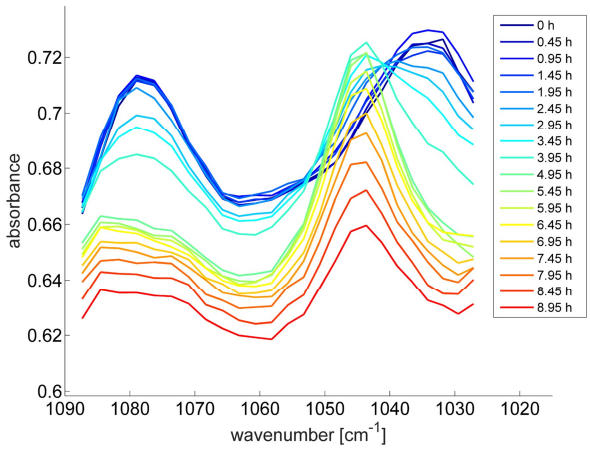

Figure 11: Time evolution of the infrared spectrum of the fermentation droplet.

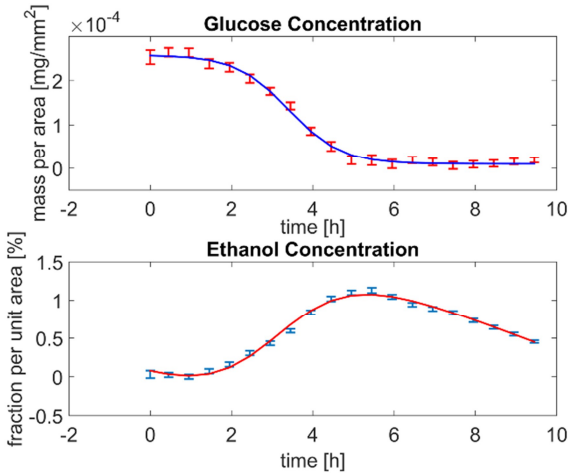

Figure 12: Results of the Pure Component Analysis of the data shown in Fig. 11.

leaky during these experiments such that the ethanol vapour could escape. This, in turn, leads to an observable loss of liquid ethanol by continued evaporation with a rate of 0.2 %/h.

When targeting a more quantitative analysis, the sample thickness must be known. Hence, we performed the second series of experiments in which we used a thin and fully filled cuvette. We thus could achieve a well-defined thickness of the liquid and were also able to quantitatively estimate the volume of CO_2 produced: A thresholding followed by a convex hull segmentation analysis of the absorbance images easily reveals the CO_2 bubble locations and their sizes (Fig. 13). The data shows that a measurable amount of ethanol is starting to be generated 1.5 h after the start, which nicely follows the expected behaviour[+++] according to the above reaction equation. After 2.5 hours, the area covered by the bubbles

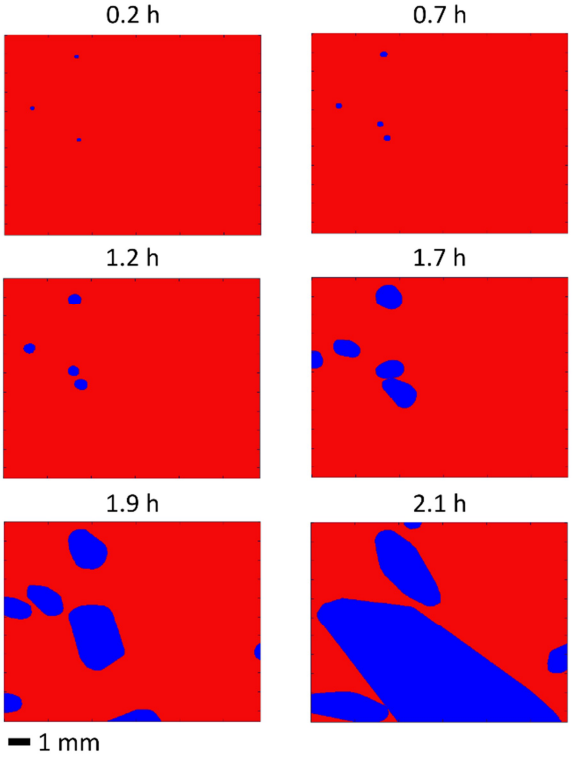

Figure 13: Evolution of the CO_2 filled bubbles (blue) over time as derived by the segmentation process.

becomes too large and prevents the further analysis of the gas volume. No ethanol leakage was evident in this experiment.

A joint analysis of the glucose, ethanol and CO_2 concentrations follows the expected behaviour (Fig. 14) and leads to a maximum glucose consumption rate of 120 mg per hour per 1 g yeast.

Conclusions

Hyperspectral imaging in the mid infrared is often hampered by signal-to-noise considerations, which finally lead to issues in speed of data acquisition, size of the object, and/or instrument cost. Since biological processes mostly take place in liquid water and since water has a large extinction coefficient in this spectral region, hyperspectral imaging of biological processes or specimen in situ is difficult to achieve.

The high spectral power density of tunable quantum cascade lasers has thus opened up a novel access to the mid-infrared hyperspectral imaging in situ and in vivo.

It is thus worthwhile to consider the obtainable signals as well as the noise limits in QCL-based mid-infrared microspectroscopy. For our setup, the optimum S/N is

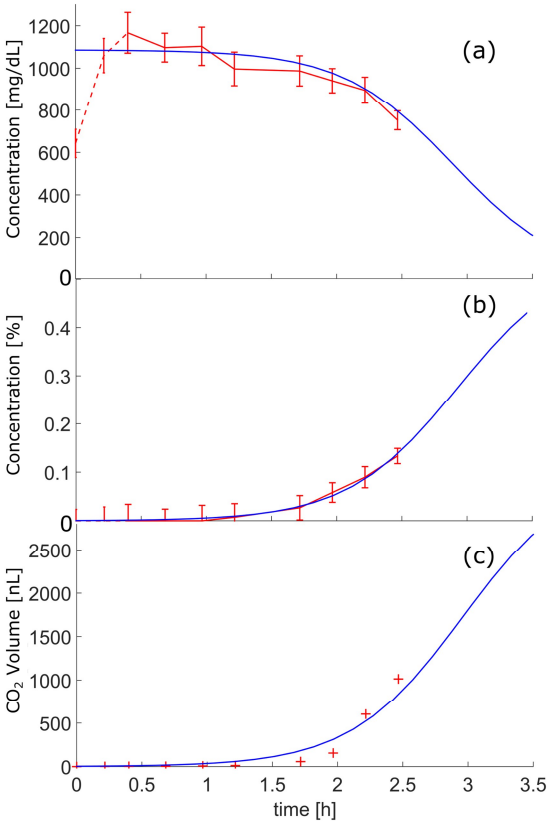

Figure 14: Time dependence of the fermentation process as derived from the pure component analysis ((a) glucose, (b) ethanol) and the area segmentation method ((c) CO_2).

achieved at path lengths around 20 µm, while S/N ratios above 10 are still maintained for water layer thicknesses well above 50 µm. The S/N improves with laser power as well as integration time and follows the expected theoretical dependence such that the whole field will benefit from e.g. future improvements in laser power.

The QCL-based microspectroscopy is exemplified by observing the fermentation process. Quantitative results for the concurrent observation of glucose consumption, alcohol production and CO_2 generation could readily be obtained and are in agreement with expectations.

Acknowledgements

The project was funded by the Baden-Württemberg Stiftung. A. Schönhals acknowledges support by the Konrad-Adenauer-Stiftung and K.Haase and A. Schönhals acknowledge support by the Heidelberg Graduate School of Fundamental Physics.

Notes and references

[+] Note that the transmission of the filled cuvette is hereby compared to the empty cuvette with just one BaF_2 window and corrected for the thickness-independent, systematic deviation of 7.4 % caused by the difference in Fresnel reflections for the BaF_2-water and BaF_2-air interfaces.

[++] If it is unknown whether this single-pixel noise will be the same for all pixels, one may wish to average this single-pixel noise over a selection of or all pixels of a transmission image. We here provide the analysis for a central area of 9 x 9 pixels unless noted otherwise.

[+++] In this experiment, the temperature had not fully stabilized during the initial 20 min.

1 M. Miljkovic, M. Romeo, C. Matthäus and M. Diem, Infrared Microspectroscopy of Individual Human Cervical Cancer (HeLa) Cells Suspended in Growth Medium, *Biopolymers*, 2004, **74**, 172-175
2 E. J. (Swain) Marcsisin, C. M. Uttero, M. Miljković and M. Diem, Infrared microspectroscopy of live cells in aqueous media, *Analyst*, 2010, **135**, 3227-3232
3 K. L. Andrew Chan, X. Niu, A. J. deMello and S. G. Kazarian, Generation of Chemical Movies: FT-IR Spectroscopic Imaging of Segmented Flows, *Anal. Chem.*, 2011, **83**, 3606-3609
4 K. L. Andrew Chan and S. G. Kazarian, FT-IR Spectroscopic Imaging of Reactions in Multiphase Flow in Microfluidic Channels, *Anal. Chem.*, 2012, **84**, 4052-4056
5 K. L. Andrew Chan and S. G. Kazarian, Aberration-free FTIR spectroscopic imaging of live cells in microfluidic devices, *Analyst*, 2013, **138**, 4040-4047
6 D. A. Moss, M. Keese and R. Pepperkok, IR microspectroscopy of live cells, *Vib. Spectrosc.*, 2005, **38**, 185-191
7 M. J. Tobin, L. Puskar, R. L. Barber, E. C. Harvey, P. Heraud, B. R. Wood, K. R. Bambery, C. T. Dillon and K. L. Munro, FTIR spectroscopy of single live cells in aqueous media by synchrotron IR microscopy using microfabricated sample holders, *Vib. Spectrosc.*, 2010, **53**, 34-38
8 K. L. Munro, K. R. Bambery, E. A. Carter, L. Puskar, M. J. Tobin, B. R. Wood and C. T. Dillon, Synchrotron radiation infrared microspectroscopy of arsenic-induced changes to intracellular biomolecules in live leukemia cells, *Vib. Spectrosc.*, 2010, **53**, 39-44
9 D. R. Whelan, K. R. Bambery, L. Puskar, D. McNaughton and B. R. Wood, Synchrotron Fourier transform infrared (FTIR) analysis of single living cells progressing through the cell cycle, *Analyst*, 2013, **138**, 3891-3899
10 M. J. Baker, J. Trevisan, P. Bassan, R. Bhargava, H. J. Butler, K. M. Dorling, P. R. Fielden, S. W. Fogarty, N. J. Fullwood, K. A. Heys, C. Hughes, P. Lasch, P. L. Martin-Hirsch, B. Obinaju, G. D. Sockalingum, J. Sulé-Suso, R. J. Strong, M. J. Walsh, B. R. Wood, P. Gardner and F. L. Martin, Using Fourier transform IR spectroscopy to analyze biological materials, *Nat. Protoc.*, 2014, **9**, 1771-1791
11 L. Quaroni and T. Zlateva, Infrared spectromicroscopy of biochemistry in functional single cells, *Analyst*, 2011, **136**, 3219-3232
12 J. Faist, F. Capasso, D. L. Sivco, C. Sirtori, A. L. Hutchinson and A. Y. Cho, Quantum Cascade Laser, *Science*, 1994, **264**, 553-556.
13 C. Vrančić, A. Fomichova, N. Gretz, C. Herrmann, S. Hoecker, A. Pucci and W. Petrich,Continuous glucose monitoring by means of mid-infrared transmission laser spectroscopy in vitro, *Analyst*, 2011, **136**, 1192-1198.
14 M. Brandstetter; L. Volgger; A. Genner; C. Jungbauer and B. Lendl, Direct determination of glucose, lactate and triglycerides in blood serum by a tunable quantum cascade laser-based mid-IR sensor, *Appl Phys B*, 2013, **110**, 233-239.

15 M. R. Alcaráz, A. Schaighofer, C. Kristament, G. Ramer, M. Brandstetter, H. Goicoechea and B. Lendl, External-Cavity Quantum Cascade Laser Spectroscopy for Mid-IR Transmission Measurements of Proteins in Aqueous Solution, *Anal. Chem.*, 2015, **87**, 6980-6987
16 C. Vrančić, N.Kröger, N. Gretz, S. Neudecker, A. Pucci and W. Petrich, A Quantitative Look Inside the Body: Minimally Invasive Infrared Analysis in Vivo, *Anal. Chem.*, 2014, **86**, 10511-10514.
17 M. C. Phillips and N. Hô, Infrared hyperspectral imaging using a broadly tunable external cavity quantum cascade laser and microbolometer focal plane array, *Opt. Express*, 2008, **16**, 1836–1845.
18 M. C. Phillips and B. E. Bernacki, Hyperspectral microscopy of explosives particles using an external cavity quantum cascade laser, *Opt. Eng.*, 2013, **52**, 061302.
19 M. R. Kole, R. K. Reddy, M. V. Schulmerich, M. K. Gelber and R. Bhargava, Discrete frequency infrared microspectroscopy and imaging with a tunable quantum cascade laser, *Anal. Chem.*, 2012, **84**, 10366–10372.
20 N. Kröger, A. Egl, M. Engel, N. Gretz, K. Haase, I. Herpich, S. Neudecker, A. Pucci, A. Schönhals and W. Petrich, Rapid hyperspectral imaging in the mid-infrared, *Proc. SPIE – Int. Soc. Opt. Eng.*, 2014, **8939**, 89390Z.
21 N. Kröger, A. Egl, M. Engel, N. Gretz, K. Haase, I. Herpich, B. Kränzlin, S. Neudecker, A. Pucci, A. Schönhals, J. Vogt and W. Petrich, Quantum cascade laser-based hyper- spectral imaging of biological tissue, *J. Biomed. Opt.*, 2014, **19**, 111607.
22 N. Kröger-Lui, N. Gretz, K. Haase, B. Kränzlin, S. Neudecker, A. Pucci, A. Regenscheit, A. Schönhals and W. Petrich, Rapid identification of goblet cells in unstained colon thin sections by means of quantum cascade laser-based infrared microspectroscopy, *Analyst*, 2015, **140**, 2086-2092
23 P. Bassan, M. J. Weida, J. Rowlette and P. Gardner, Large scale infrared imaging of tissue micro arrays (TMAs) using a tunable Quantum Cascade Laser (QCL) based micro- scope, Analyst, 2014, 139, 3856.
24 K. Yeh, S. Kenkel, J.-N. Liu and R. Bhargava, Fast Infrared Chemical Imaging with a Quantum Cascade Laser, *Anal. Chem.*, 2015, **87**, 485-493.
25 K. Haase, N. Kröger-Lui, A. Pucci, A. Schönhals and W. Petrich, Real-time mid-infrared imaging of living microorganisms, J. Biophotonics, 2015, DOI: 10.1002/jbio.201500264. (In press, first published online 17 Nov 2015)
26 P. Lasch and W. Petrich, Data Acquisition and Analysis in Biomedical Vibrational Spectroscopy, in Biomedical Applications of Synchrotron Infrared Microspectroscopy: A Practical Approach, RSC Analytical Spectroscopy Series v. 11, ed. D. Moss, Royal Society of Chemistry, Cambridge, UK, 2010, 192–225.
27 G. M. Hale and M. R. Querry, Optical Constants of Water in the 200-nm to 200-microm Wavelength Region, Appl. Opt., 1973, **12**, 555–563.
28 C. Herrmann, C. Vrančić, A. Fomichova, N. Gretz, S. Hoecker, A. Pucci and W. Petrich, In-vitro characteristics of a mid-infrared, continuous glucose sensor, *Proc. SPIE – Int. Soc. Opt. Eng.*, 2010, **8219**, 75600E.